Lawrence Berkeley National Laboratory
Recent Work

Title
Giant spin-splitting and gap renormalization driven by trions in single-layer WS 2 /h-BN heterostructures

Permalink
https://escholarship.org/uc/item/5xh1q06m

Journal
Nature Physics, 14(4)

ISSN
1745-2473

Authors
Katoch, J
Ulstrup, S
Koch, RJ
et al.

Publication Date
2018-04-01

DOI
10.1038/s41567-017-0033-4

Peer reviewed

eScholarship.org Powered by the California Digital Library
University of California

nature physics

LETTERS

https://doi.org/10.1038/s41567-017-0033-4

Giant spin-splitting and gap renormalization driven by trions in single-layer WS_2/h-BN heterostructures

Jyoti Katoch[1], Søren Ulstrup[2,3], Roland J. Koch[2], Simon Moser[2], Kathleen M. McCreary[4], Simranjeet Singh[1], Jinsong Xu[1], Berend T. Jonker[4], Roland K. Kawakami[1], Aaron Bostwick[2], Eli Rotenberg[2] and Chris Jozwiak[2*]

In two-dimensional (2D) semiconducting transition metal dichalcogenides (TMDs), new electronic phenomena such as tunable bandgaps[1-3] and strongly bound excitons and trions emerge from strong many-body effects[4-6], beyond the spin and valley degrees of freedom induced by spin–orbit coupling and by lattice symmetry[7]. Combining single-layer TMDs with other 2D materials in van der Waals heterostructures offers an intriguing means of controlling the electronic properties through these many-body effects, by means of engineered interlayer interactions[8-10]. Here, we use micro-focused angle-resolved photoemission spectroscopy (microARPES) and in situ surface doping to manipulate the electronic structure of single-layer WS_2 on hexagonal boron nitride (WS_2/h-BN). Upon electron doping, we observe an unexpected giant renormalization of the spin–orbit splitting of the single-layer WS_2 valence band, from 430 meV to 660 meV, together with a bandgap reduction of at least 325 meV, attributed to the formation of trionic quasiparticles. These findings suggest that the electronic, spintronic and excitonic properties are widely tunable in 2D TMD/h-BN heterostructures, as these are intimately linked to the quasiparticle dynamics of the materials[11-13].

Coulomb interactions in 2D materials are several times stronger than in their 3D counterparts. In 2D TMDs, this is most directly evidenced by the presence of excitons with binding energies an order of magnitude higher than in the bulk[4]. Although the excitons in these 2D materials have been widely studied by optical techniques[13], the impact of strong electron–electron interactions on the quasiparticle band structure remains unclear. Theory predicts that many-body effects will influence the spin–orbit splitting around the valence-band maximum (VBM) and conduction-band minimum (CBM)[14]. Although these should be observable by ARPES, a direct probe of many-body effects[15], measurements so far have mainly focused on the layer-dependence of the single-particle spectrum and the direct bandgap transition in 2D TMD systems, including epitaxial single-layer $MoSe_2$ (ref. [16]) and single-layer WSe_2 (ref. [17]) grown on doped multilayer graphene, and single-layer MoS_2 grown on a metal surface[18]. On such conductive substrates, the interfacial interactions and screening are known to strongly influence the electronic properties of the single-layer TMD[9].

Flakes of single-layer TMDs have been transferred onto oxide substrates such as SiO_2, where the substrate screening and interfacial effects are potentially reduced. However, resulting ARPES spectra have been too broad for detailed analysis[19], probably owing to surface roughness and charge impurity scattering[20]. Compared with SiO_2 and similar substrates, h-BN has favourable qualities such as atomic flatness, modest screening and a homogeneous charge distribution. This should enable direct investigation of the intrinsic electronic structure and many-body effects of the adjacent TMD. Hexagonal BN is often used as a substrate for graphene heterostructures[8,20] with high device performance[21] and new exotic electronic states such as quantized Dirac cones[22]. Unfortunately, the lateral size of mechanically assembled heterostructures is usually of the order of 10 μm, much smaller than the beam spot of typical ARPES setups (≳100 μm). Furthermore, sample charging on insulating bulk h-BN substrates would complicate ARPES experiments.

We overcome these challenges as follows. We realize a high-quality 2D semiconductor–insulator interface by mechanically transferring a relatively large (~100 μm) single-layer WS_2 crystal onto a thin flake of h-BN that has itself been transferred onto a degenerately doped TiO_2 substrate, as depicted in Fig. 1a. Sample charging is avoided because there is electrical contact from the continuous single-layer WS_2 flake to both the h-BN and the conductive TiO_2. Figure 1b is an optical microscope image of the sample, including a flake of h-BN, approximately 100 μm wide, surrounded by several transferred flakes of single-layer WS_2 on the TiO_2 substrate (WS_2/TiO_2), one of which partially overlaps the h-BN.

By using a state-of-the-art spatially resolved microARPES experiment with a 10 μm focused synchrotron beam spot, we are able to collect distinct high-quality band-structure information from the multiple micrometre-scale interfaces. A spatial map of the photoemission intensity around the WS_2/h-BN heterostructure is shown in Fig. 1c, which was produced by integrating the intensity over the boxed region of the corresponding k-space band structure shown in Fig.1d, measured at each spatial point. The crossing single-layer WS_2 and h-BN bands in this region ensure strong contrast between WS_2/h-BN (white arrow), regions of WS_2/TiO_2 (light purple) and regions of bare TiO_2 (dark purple) in the spatial map. The photoemission map (Fig. 1c) corresponds directly to the optical micrograph (Fig. 1b) with contrasts that reflect the intensity of the WS_2 and h-BN features in the red box in Fig. 1d. The band structures from bare TiO_2, WS_2/TiO_2 and several spots within the WS_2/h-BN heterostructure are presented in Supplementary Fig. 1. The slight intensity

[1]Department of Physics, The Ohio State University, Columbus, OH, USA. [2]Advanced Light Source, Lawrence Berkeley National Laboratory, Berkeley, CA, USA. [3]Department of Physics and Astronomy, Interdisciplinary Nanoscience Center (iNANO), Aarhus University, Aarhus C, Denmark. [4]Naval Research Laboratory, Washington, DC, USA. Jyoti Katoch and Søren Ulstrup contributed equally to this work. *e-mail: cmjozwiak@lbl.gov

© 2018 Macmillan Publishers Limited, part of Springer Nature. All rights reserved.

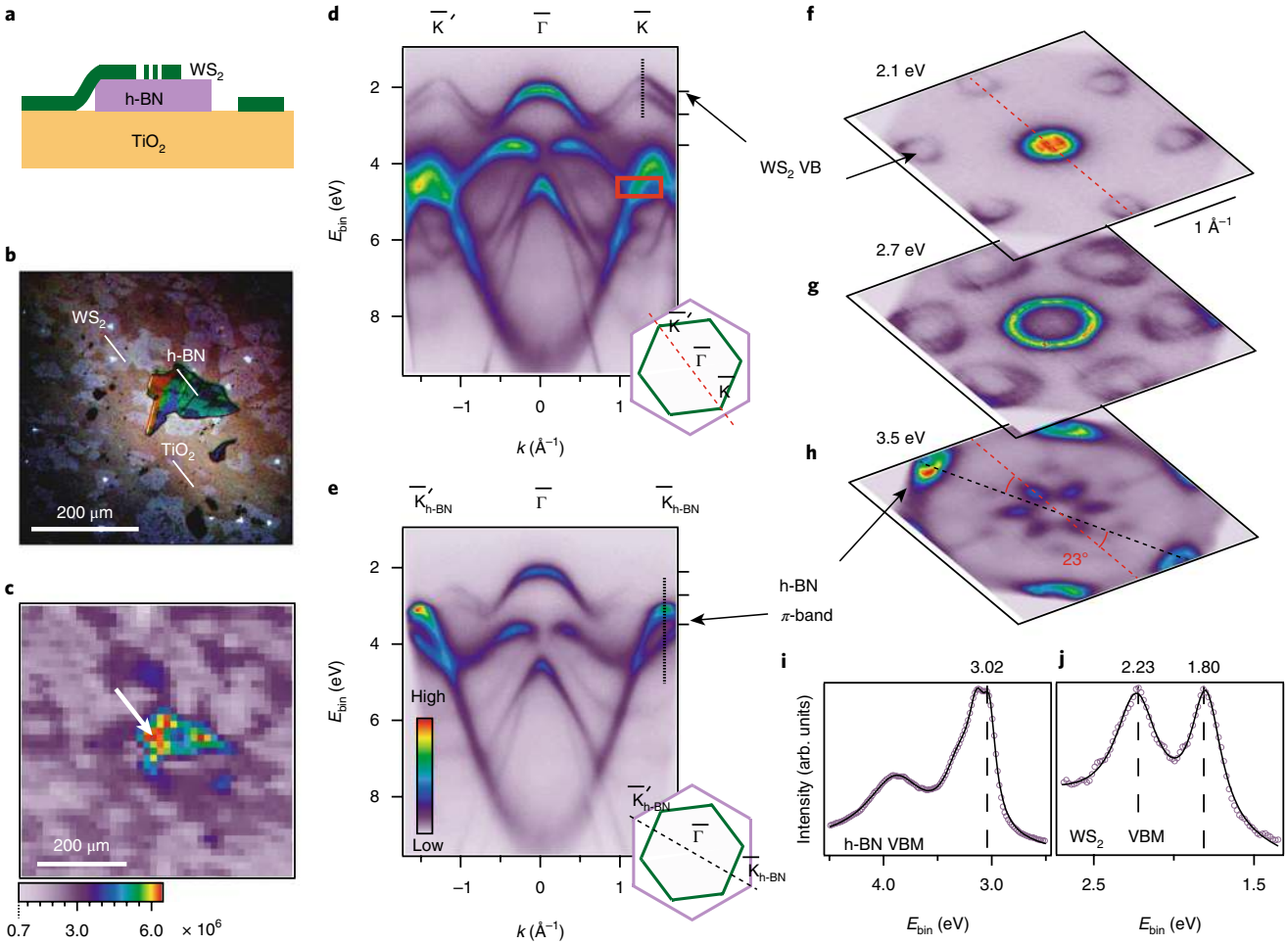

Fig. 1 | Spatially resolved electronic structure mapping of a WS_2/h-BN heterostructure supported on TiO_2. a, Side-view sketch of WS_2/h-BN on TiO_2, illustrating single-layer WS_2 regions with direct contacts to h-BN and to TiO_2. **b**, Optical microscope image of the sample. The contrast has been strongly enhanced for better visualization of the single-layer WS_2. Brown patches correspond to bare TiO_2, light purple to WS_2/TiO_2 and the darker green/red structure is the h-BN flake. **c**, Spatial map of photoemission intensity (integrated over the red box in **d**) for the same region seen in **b**. See Supplementary Section 1 for details on the spatial intensity variations. **d**, Measured dispersion along the $\overline{K}$–$\overline{\Gamma}$–$\overline{K}'$ direction of the single-layer WS_2 Brillouin zone (see green Brillouin zone and dashed red line in the insert) collected at the spatial coordinates marked by a white arrow in **c**. The rectangular red box marks a region with crossing WS_2 and h-BN bands where the photoemission intensity is integrated to produce the spatial map in **c**. **e**, ARPES dispersion in the high-symmetry direction of h-BN (see purple Brillouin zone and dashed black line in the insert). **f**–**h**, Constant energy cuts obtained at the given binding energies (see also ticks on the right of panels **d**,**e**). Arrows mark distinct energy contours relating to single-layer WS_2 and to h-BN. The red and black dashed lines (insert in **d**,**e**) indicate a twist angle of (23 ± 1)° in between the single-layer WS_2 and h-BN. VB, valence band. **i**,**j**, EDCs obtained along the dotted lines in **d**,**e** around the h-BN VBM (**i**) and single-layer WS_2 VBM (**j**). The positions of the band edges are given in units of eV and the error bar is 30 meV (and thus smaller than the symbol size).

variations within the WS_2/h-BN heterostructure arise from areas with pinholes introduced in the single-layer WS_2 during transfer[23], as sketched in Fig. 1a. The sensitivity towards such features, which are not resolved by the optical micrograph, demonstrates the ability to identify optimum sample areas directly in the ARPES experiment, which is critical for such complex, heterogeneous samples.

The valence-band electronic structure through the entire first Brillouin zone of the heterostructure, including the single-layer WS_2 bands and the π-band dispersion of the underlying h-BN, is shown in Fig. 1d,e. The data are collected from a single spatial point where the WS_2 features are most intense (white arrow in Fig. 1c). Custom electrostatic deflectors mounted in the photoelectron analyser enable full scans of k-space at exactly this position without any drift from sample motion. The Brillouin zone orientations and twist angle between the two materials are determined from the constant binding energy cuts shown in Fig. 1f–h. From the relative orientation of the hole pockets, we estimate a twist angle of (23 ± 1)°. The energy distribution curves (EDCs) in Fig. 1i,j track the VBM binding-energy positions of the two materials. The upper valence band of single-layer WS_2 is located inside the bandgap of h-BN and the single-layer WS_2 VBM is characterized by a spin–orbit splitting of 430 meV (see Fig. 1j), in agreement with theoretical predictions[12] and previous experiments[23,24]. The clear electronic states and lack of band hybridization reveal a weak interlayer interaction between the two materials. Similar to work[22] on graphene/h-BN, we expect these data to represent the intrinsic electronic structure of single-layer WS_2 with negligible substrate influence.

The impact of electron doping on the electronic structure through in situ surface potassium deposition is shown in Fig. 2a,b (see Supplementary Fig. 2 for core level data on clean and potassium-dosed samples). Doping WS_2/h-BN leads to the CBM being populated at the $\overline{K}$ points of single-layer WS_2, confirming the expected direct bandgap. A surprising change of the dispersion of the two spin–orbit-split valence bands VB_A and VB_B

© 2018 Macmillan Publishers Limited, part of Springer Nature. All rights reserved.

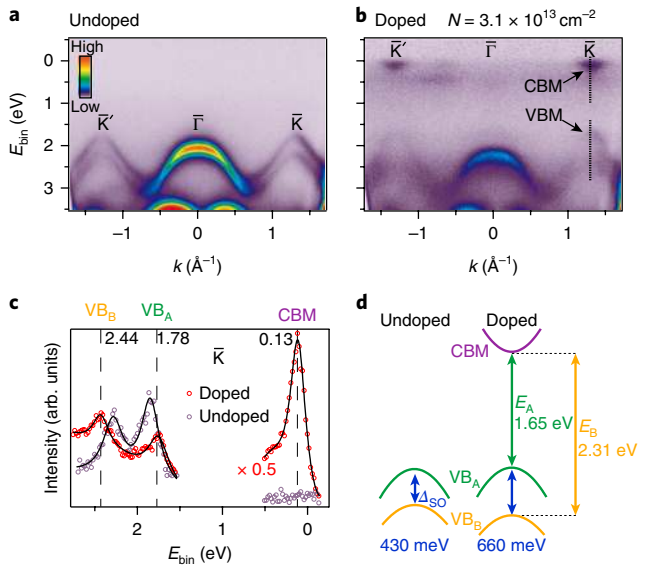

Fig. 2 | Electronic structure of strongly electron-doped WS_2/h-BN. a, Dispersion of single-layer WS_2/h-BN along the $\overline{K}$-$\overline{\Gamma}$-$\overline{K}'$ direction of the single-layer WS_2 Brillouin zone, collected from the spot marked by the white arrow in Fig. 1c. **b**, Corresponding data at the highest achieved electron-doping N. **c**, EDCs (markers) around the VBM and CBM at $\overline{K}$ (see dotted lines and arrows in **b**) for undoped and electron-doped single-layer WS_2 on h-BN. Peak positions extracted from Lorentzian line fits (curves) are shown as vertical dashed lines, and values for the doped case are given in units of eV. Note that the CBM intensity has been scaled by a factor of 0.5 for clearer comparison with the other peaks. **d**, Schematics of the dispersion change of the valence-band spin–orbit split bands VB_A and VB_B due to doping and the measured energy gaps between the CBM and VB_A (denoted as E_A) and VB_B (denoted as E_B) in the doped case. The energy splitting due to spin–orbit coupling, Δ_{SO}, and the values of E_A and E_B are provided with error bars of 30 meV.

of WS_2/h-BN around the $\overline{K}$ point is observed, highlighted in the EDCs in Fig. 2c. The spin-splitting due to spin–orbit coupling Δ_{SO} increases from 430 meV in the undoped case to 660 meV in the electron-doped case, as sketched in Fig. 2d. Such a large spin-splitting has not previously been observed in any single-layer material to our knowledge. In this case, the bandgap of single-layer WS_2 is 1.65 eV and the CBM to VB_B offset is 2.31 eV. These values are sketched in Fig. 2d and denoted as E_A and E_B, respectively, owing to the relation with the A and B exciton lines observed in optical experiments[5].

A detailed evolution of the band extrema with increasing doping is shown in Fig. 3a–e. The dispersions around the VBM as determined from EDC line shape analysis (see Supplementary Fig. 6) are shown by dashed red curves and directly compared in Fig. 3f. We estimate the charge carrier density, N, at each dosing step from the CBM position (see Methods). These estimated doping levels are consistent with those achieved in similar experiments[25] on bulk WSe_2 and with the intensity of the potassium 3p core level (see Supplementary Fig. 3).

From EDC peak positions at $\overline{K}$ (see Supplementary Fig. 7), we extract the VBM and CBM energies as a function of dosing (Fig. 3g). After the first dosing step ($N = 1.7 \times 10^{13}$ cm^{-2}), the CBM becomes occupied, and VB_A and VB_B rigidly shift to higher binding energy. With further dosing, the CBM moves further down to higher binding energy, while VB_A and VB_B shift back towards lower binding energy, resulting in a continuous narrowing of the bandgap. In particular, the dispersion of VB_A appears to renormalize with increased doping (see Fig. 3d–f), with a strong increase in Δ_{SO} (Fig. 3g,h). This leads to a corresponding change in the relative energy separation between E_A and E_B (Fig. 3i), implying that the energies of the A and B exciton lines also separate. Data points with different marker shapes and colours in Fig. 3h,i stem from separate doping experiments on the three different flakes studied in Figs. 2 and 3 and in Supplementary Fig. 8. A reproducible trend is found across all flakes. Note also that in the carrier density range between 2×10^{12} cm^{-2} and 1.0×10^{13} cm^{-2}, we find a more modest bandgap renormalization of (90 ± 30) meV, which is in excellent agreement with gated device measurements on a similar sample[1]. Our observations reveal that it is insufficient to consider only rigid band shifts, and that strong dispersion changes can result from doping of single-layer TMDs.

The surprising doping-induced changes in Δ_{SO} are probably not directly related to the surface potential induced by the potassium deposition (through, for example, the Rashba interaction), which is not expected to affect Δ_{SO} at $\overline{K}$ for single-layer TMDs. This would introduce a splitting at $\overline{\Gamma}$, which we do not observe[26,27]. Furthermore, we can rule out any potassium-induced structural symmetry breaking in our heterostructure, as only minor rigid binding-energy shifts of the S 2p core levels of WS_2 and of the underlying h-BN π-band are observed after complete doping (see Supplementary Figs. 4 and 5). The reproducible charge carrier dependence of the spectral changes demonstrated in Figs. 2 and 3 and Supplementary Fig. 8 suggests that these changes originate from Coulomb interactions around the band extrema of single-layer WS_2 (refs [1,2,14]).

The linewidths of the VB_A and CBM peaks exhibit a non-monotonic dependence on doping, which cannot be described by simple scattering on ionized potassium impurities (see further discussion in Supplementary Section 4). Specifically, the observation that VB_A renormalization coincides with occupation of the CBM suggests that the renormalization is caused by new scattering channels available upon occupation of the conduction band. Previous works using surface potassium deposition for electron-doping of single-layer TMDs on conductive substrates[16–18], where the Coulomb interactions are already strongly screened in the undoped case[9], have shown no such changes in Δ_{SO}. We believe that the reduced dielectric constant of the h-BN substrate plays a key role for these observations as it leads to reduced screening of the many-body interactions in the bare single-layer WS_2.

An alkali-atom-induced renormalization of the valence band edge at K towards E_F, observed in several bulk TMDs, has been attributed to the breaking of the degeneracy of the outermost layers by the doping-induced field[25,28]. This can either be a single-particle effect[28] or a combination of single- and many-body effects[25], the latter of which suggests a negative electronic compressibility (NEC), the motion of the chemical potential μ towards the VBM, i.e. $d\mu/dN < 0$.

In contrast, we observe distinctive effects in single-layer WS_2/h-BN, namely (1) a renormalization of Δ_{SO} within the single layer, (2) an NEC in which $|d\mu/dN|$ is significantly larger than in the bulk[25,28], and (3) a VB_A slope that is discontinuous at $k = (\overline{K}, \overline{K}') \pm \sim 0.15$ Å^{-1} in Fig. 2b at high doping. This leads to kinks in VB_A, exemplified by the arrow in Fig. 3e, which develop continuously in strength with doping in Fig. 3a–e. Such kinks are common in ARPES when the created 'photohole' interacts strongly with well-defined (in energy and/or momentum) excitations[15].

As noted above, the band renormalization coincides with the occupation of the conduction band, suggesting that such excitations are associated with electron–hole (e–h) pairs near E_F in the conduction band, induced in response to the valence-band hole created during photoemission. In the undoped situation sketched in Fig. 4a, such interactions are not possible. At high carrier densities where the conduction band is occupied, an e–h excitation around $\overline{K}$ (or $\overline{K}'$) can interact with the valence-band photohole, forming a positively charged, bound electron–hole–hole complex denoted as

© 2018 Macmillan Publishers Limited, part of Springer Nature. All rights reserved.

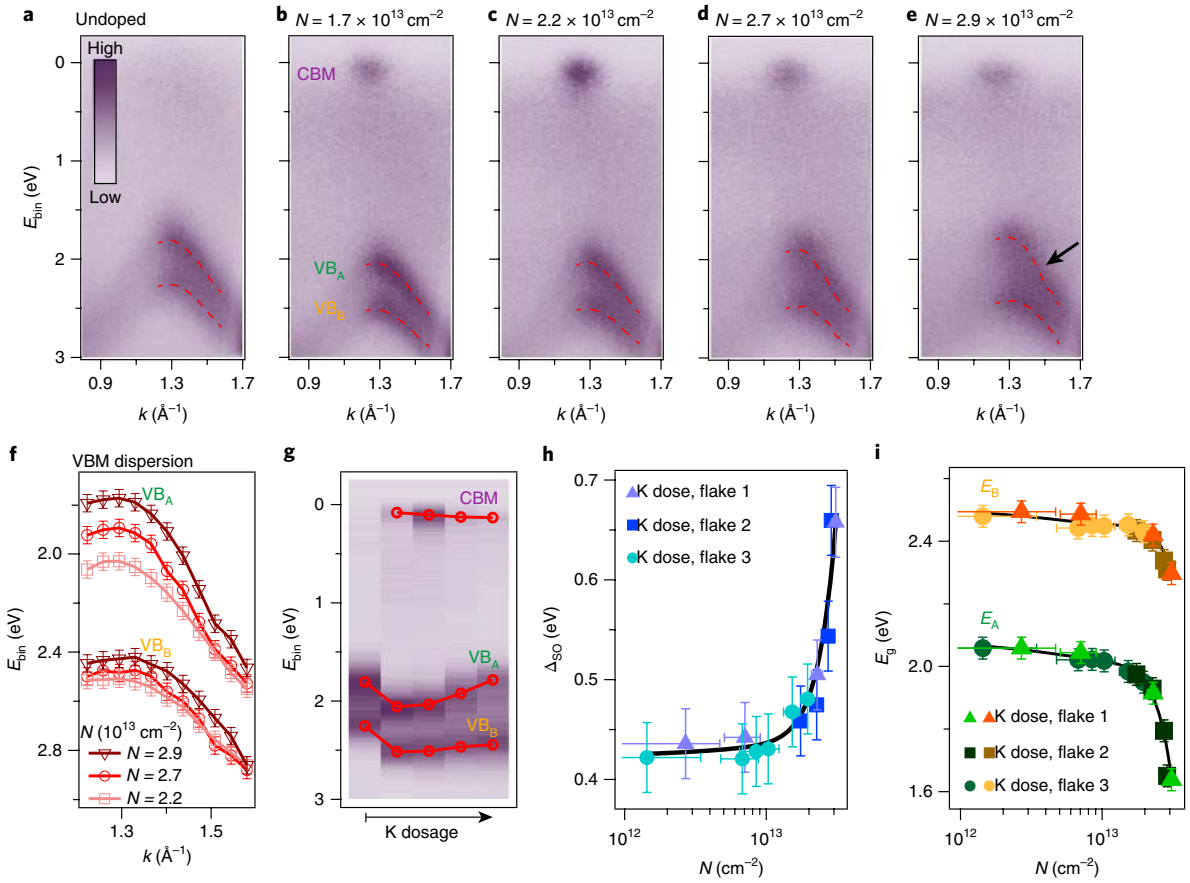

Fig. 3 | Evolution of single-layer WS_2 VBM and CBM dispersion with charge-carrier density. a–e, microARPES measurements around the $\overline{K}$-point of single-layer WS_2/h-BN for clean (**a**) and increasingly potassium-dosed cases (**b–e**). The red curves are the fitted VB_A and VB_B dispersions determined from double Lorentzian fits of EDCs (see Supplementary Fig. 6). The arrow in **e** points to a possible kink in VB_A. **f**, VB_A and VB_B dispersions extracted from the EDC analysis in the strongly electron-doped cases. **g**, ARPES intensity at the $\overline{K}$-point and peak positions (red markers) at each potassium-dosing step (see corresponding EDC analysis in Supplementary Fig. 7). **h,i**, Spin–orbit splitting (**h**) and bandgap values (**i**) determined from the VB_A, VB_B and CBM positions, combining data from K-doping experiments on the different WS_2/h-BN flakes investigated here, in Fig. 2 and in Supplementary Fig. 8. The lines in **h,i** are provided as guides to the eye. N, charge carrier density. E_g, bandgap energy.

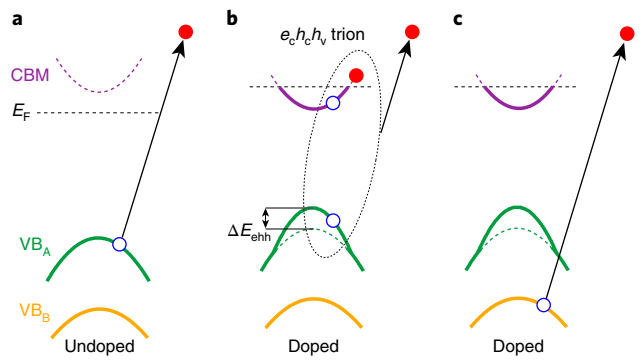

Fig. 4 | Quasiparticle dynamics in doped single-layer WS_2. a, Band diagram illustrating the generated photohole (open blue circle) in VB_A and the photoemitted free electron (filled red circle) in the undoped situation. **b**, Illustration of an $e_c h_c h_v$ trionic quasiparticle generated in doped single-layer WS_2. The photohole binding energy is lowered and the VB_A dispersion renormalizes with respect to the bare band (green dashed curve) by the trion binding energy ΔE_{ehh}. **c**, A photohole generated in VB_B in the doped situation undergoes a process that is analogous to the undoped situation in **a**, owing to the absence of strong trion interactions with photoholes in this band.

$e_c h_c h_v$, where (c, v) denotes charges in the (conduction band, valence band), respectively, as illustrated in Fig. 4b. Such a process would renormalize the bare band dispersion and lifetime of the valence-band states, broadening and shifting their spectra as observed.

These excitations may be compared to the X^+ (X^-) trions found in p- (n)-doped TMDs with configuration $e_c h_v h_v$ ($e_c e_c h_v$). Such trions have been invoked to interpret additional spectral lines shifted in energy by ~20–60 meV with respect to the main A exciton line in optical absorption[6] and luminescence[6,29] measurements of single-layer TMDs. Our measurements show a relative shift of VB_A by ~0.23 eV compared with VB_B, which reflects the absolute binding-energy reduction ΔE_{ehh} of the photohole associated with the formation of the trion (see Fig. 4b). The order of magnitude of ΔE_{ehh} is compatible with the absolute trion binding energies that can be extracted from the optical experiments[6,29], but the exact values are expected to depend on the dielectric environment of the sample and the doping. So far, corresponding trion features associated with B excitons have not been observed in optical experiments, which is fully consistent with the absence of renormalization of the VB_B dispersion in the present ARPES data, as seen in Fig. 3a–e and as sketched in Fig. 4c. This lack of renormalization of the VB_B dispersion might be attributed to additional decay channels of the VB_B hole such as decay into the VB_A band. The strong increase in Δ_{SO} and the bandgap renormalization can therefore be viewed as direct

© 2018 Macmillan Publishers Limited, part of Springer Nature. All rights reserved.

consequences of forming trionic quasiparticles around the VB_A and conduction-band extrema.

The assignment of trions in optical measurements of semiconducting TMDs is currently being debated, as a recent theoretical study points towards the possibility of interactions between e–h pairs and the remaining charge density forming other types of quasiparticles such as exciton-polarons[30]. Our ARPES measurements provide direct evidence for such multi-component excitations in single-layer TMDs and give access to both their energy and momentum dependence that is lacking from momentum-integrating transport, optical or tunnelling measurements. We envisage further theoretical and experimental studies to disentangle such many-body effects in the spectral function of single-layer TMDs. The charge-carrier-dependent electronic bandgap and spin-splitting that arise from these many-body effects will profoundly impact the charge-, spin- and valley-dependent dynamics and transport properties of devices, as well as the interpretation of excitonic effects.

Received: 26 April 2017; Accepted: 7 December 2017;
Published online: 22 January 2018

References

1. Chernikov, A. et al. Electrical tuning of exciton binding energies in monolayer WS_2. *Phys. Rev. Lett.* **115**, 126802 (2015).
2. Liang, Y. & Yang, L. Carrier plasmon induced nonlinear band gap renormalization in two-dimensional semiconductors. *Phys. Rev. Lett.* **114**, 063001 (2015).
3. Chernikov, A., Ruppert, C., Hill, H., Rigosi, A. & Heinz, T. Population inversion and giant bandgap renormalization in atomically thin WS_2 layers. *Nat. Photon.* **9**, 466–470 (2015).
4. Ramasubramaniam, A. Large excitonic effects in monolayers of molybdenum and tungsten dichalcogenides. *Phys. Rev. B* **86**, 115409 (2012).
5. Qiu, D., Jornada, F. & Louie, S. Optical spectrum of MoS_2: many-body effects and diversity of exciton states. *Phys. Rev. Lett.* **111**, 216805 (2013).
6. Mak, K. F. et al. Tightly bound trions in monolayer MoS_2. *Nat. Mater.* **12**, 207–211 (2013).
7. Xiao, D., Liu, G., Feng, W., Xu, X. & Yao, W. Coupled spin and valley physics in monolayers of MoS_2 and other Group-VI dichalcogenides. *Phys. Rev. Lett.* **108**, 196802 (2012).
8. Geim, A. & Grigorieva, I. Van der Waals heterostructures. *Nature* **499**, 419–425 (2013).
9. Ugeda, M. et al. Giant bandgap renormalization and excitonic effects in a monolayer transition metal dichalcogenide semiconductor. *Nat. Mater.* **13**, 1091–1095 (2014).
10. Larentis, S. et al. Band offset and negative compressibility in graphene–MoS_2 heterostructures. *Nano Lett.* **14**, 2039–2045 (2014).
11. Xu, X., Yao, W., Xiao, D. & Heinz, T. Spin and pseudospins in layered transition metal dichalcogenides. *Nat. Phys.* **10**, 343–350 (2014).
12. Kormányos, A. k·p theory for two-dimensional transition metal dichalcogenide semiconductors. *2D Mater.* **2**, 049501 (2015).
13. Mak, K. F. & Shan, J. Photonics and optoelectronics of 2D semiconductor transition metal dichalcogenides. *Nat. Photon.* **10**, 216–226 (2016).
14. Ferreiros, Y. & Cortijo, A. Large conduction band and Fermi velocity spin splitting due to Coulomb interactions in single-layer MoS_2. *Phys. Rev. B* **90**, 195426 (2014).
15. Bostwick, A., Ohta, T., Seyller, T., Horn, K. & Rotenberg, E. Quasiparticle dynamics in graphene. *Nat. Phys.* **3**, 36–40 (2007).
16. Zhang, Y. et al. Direct observation of the transition from indirect to direct bandgap in atomically thin epitaxial $MoSe_2$. *Nat. Nanotechnol.* **9**, 111–115 (2014).
17. Zhang, Y. et al. Electronic structure, surface doping, and optical response in epitaxial WSe_2 thin films. *Nano Lett.* **16**, 2485–2491 (2016).
18. Miwa, J. et al. Electronic structure of epitaxial single-layer MoS_2. *Phys. Rev. Lett.* **114**, 046802 (2015).
19. Jin, W. et al. Direct measurement of the thickness-dependent electronic band structure of MoS_2 using angle-resolved photoemission spectroscopy. *Phys. Rev. Lett.* **111**, 106801 (2013).
20. Dean, C. et al. Boron nitride substrates for high-quality graphene electronics. *Nat. Nanotechnol.* **5**, 722–726 (2010).
21. Wang, L. et al. One-dimensional electrical contact to a two-dimensional material. *Science* **342**, 614–617 (2013).
22. Wang, E. et al. Gaps induced by inversion symmetry breaking and second-generation Dirac cones in graphene/hexagonal boron nitride. *Nat. Phys.* **12**, 1111–1115 (2016).
23. Ulstrup, S. et al. Spatially resolved electronic properties of single-layer WS_2 on transition metal oxides. *ACS Nano* **10**, 10058–10067 (2016).
24. Dendzik, M. et al. Growth and electronic structure of epitaxial single-layer WS_2 on Au(111). *Phys. Rev. B* **92**, 245442 (2015).
25. Riley, J. et al. Negative electronic compressibility and tunable spin splitting in WSe_2. *Nat. Nanotechnol.* **10**, 1043–1047 (2015).
26. Yuan, H. et al. Zeeman-type spin splitting controlled by an electric field. *Nat. Phys.* **9**, 563–569 (2013).
27. Shanavas, K. V. & Satpathy, S. Effective tight-binding model for MX_2 under electric and magnetic fields. *Phys. Rev. B* **91**, 235145 (2015).
28. Kang, M. et al. Universal mechanism of band-gap engineering in transition-metal dichalcogenides. *Nano Lett.* **17**, 1610–1615 (2017).
29. Zhu, B., Chen, X. & Cui, X. Exciton binding energy of monolayer WS_2. *Sci. Rep.* **5**, 9218 (2015).
30. Efimkin, D. K. & MacDonald, A. H. Many-body theory of trion absorption features in two-dimensional semiconductors. *Phys. Rev. B* **95**, 035417 (2017).

Acknowledgements

We thank A. H. MacDonald for discussions. S.U. acknowledges financial support from the Danish Council for Independent Research, Natural Sciences, under the Sapere Aude programme (grant no. DFF-4090-00125) and from VILLUM FONDEN (grant no. 15375). R.J.K. is supported by a fellowship within the postdoctoral programme of the German Academic Exchange Service (DAAD). S.M. acknowledges support by the Swiss National Science Foundation (grant no. P2ELP2-155357). The work at Ohio State was primarily supported by NSF-MRSEC (grant DMR-1420451). Work at the US Naval Research Laboratory (NRL) was supported by core programmes and the NRL Nanoscience Institute, and by the Air Force Office of Scientific Research under contract number AOARD 14IOA018- 134141. This research used resources of the Advanced Light Source, which is a US Department of Energy Office of Science User Facility under contract no. DE-AC02-05CH11231.

Author contributions

J.K. and S.U. conceived and planned the experiments. K.M.M. and B.T.J. synthesized the single-layer WS_2 flakes on SiO_2. J.K., S.S., J.X. and R.K.K. assembled the WS_2/h-BN heterostructures on TiO_2. S.U., R.J.K., S.M., J.K., A.B., E.R. and C.J. performed the microARPES experiments. The microARPES set-up was developed and maintained by C.J., A.B. and E.R. S.U. analysed the experimental data with inputs from C.J. and E.R. All authors contributed to the interpretation and writing of the manuscript.

Competing interests

The authors declare no competing financial interests.

Additional information

Supplementary information is available for this paper at https://doi.org/10.1038/s41567-017-0033-4.

Reprints and permissions information is available at www.nature.com/reprints.

Correspondence and requests for materials should be addressed to C.J.

Publisher's note: Springer Nature remains neutral with regard to jurisdictional claims in published maps and institutional affiliations.

© 2018 Macmillan Publishers Limited, part of Springer Nature. All rights reserved.

Methods

Fabrication of WS_2/h-BN heterostructures. The heterostructures were prepared by successively transferring few-layer h-BN (commercial crystal from HQ Graphene) and then single-layer WS_2 onto 0.5 wt% Nb-doped rutile TiO_2(100) (Shinkosha Co., Ltd). A thin film of polycarbonate (PC) was mounted onto polydimethylsiloxane (PDMS) on a glass slide to prepare a PC/PDMS stamp. This stamp was first used to pick up h-BN flakes from a SiO_2 substrate and then dropped onto the TiO_2 substrate under a microscope. The transferred h-BN flakes were cleaned of any polymer residue by annealing at 625 K in ultrahigh vacuum (UHV) for 1 h. Next, single-layer WS_2 flakes were picked up from the SiO_2 growth substrate and aligned to drop onto h-BN, such that a part of the flake made contact with the TiO_2 substrate. The process was followed by another annealing step in UHV to clean off any remaining residues.

Experimental details of microARPES. The samples were transported through air to the Microscopic and Electronic Structure Observatory (MAESTRO) at the Advanced Light Source where they were inserted in the microARPES UHV end-station with a base pressure better than 5×10^{-11} mbar. The samples were given a mild anneal at 600 K prior to measurements, in order to desorb adsorbates from air. The synchrotron beam-spot size was on the order of 10 µm for the photon energies of 145 eV and 76.5 eV used to obtain the microARPES data. The data were collected using a hemispherical Scienta R4000 electron analyser equipped with custom-made deflectors that enable collecting ARPES spectra over a full Brillouin zone without moving the sample. Potassium-dosing experiments were carried out by evaporating potassium in situ from a SAES getter source mounted in the analysis chamber such that dosing is performed in an optimum sample measurement position without moving the sample. Core level data of undoped and potassium-dosed samples are presented in Supplementary Fig. 2 to document the cleanliness of the samples. The data in Figs. 1 and 2 are from the same sample, whereas the data in Fig. 3 and Supplementary Fig. 8 were obtained on fresh samples. The charge carrier density N is estimated using a simple model of a 2D parabolic band given by $N=\left(g_v g_s m^*_{cb} k_B T / 2\pi\hbar^2\right)\ln(1+e^{E-E_F/k_B T})$, where the factors $g_v=2$ and $g_s=2$ take spin- and valley-degeneracy into account, m^*_{cb} is the effective mass of the single-layer WS_2 conduction band obtained from ref. [12], k_B is Boltzmann's constant, $\hbar$ is the reduced Planck constant, T is the sample temperature and $E-E_F$ is determined from the fitted CBM position. The total energy resolution and momentum resolution in the microARPES data were better than 20 meV and 0.01 $Å^{-1}$, respectively. Measurements and dosing experiments were carried out at both 85 K and at 20 K, without any noticeable change in behaviour between the two temperatures.

Data availability. The data that support the plots within this paper and other findings of this study are available from the corresponding author upon reasonable request.

© 2018 Macmillan Publishers Limited, part of Springer Nature. All rights reserved.